Nanoscale

RSC Publishing

PAPER

Coexistence of plasmonic and magnetic properties in $Au_{89}Fe_{11}$ nanoalloys†

Cite this: *Nanoscale*, 2013, **5**, 5611

Vincenzo Amendola,*[a] Moreno Meneghetti,[a] Osman M. Bakr,[b] Pietro Riello,[c] Stefano Polizzi,[c] Dalaver H. Anjum,[d] Stefania Fiameni,[e] Paolo Arosio,[f] Tomas Orlando,[g] Cesar de Julian Fernandez,[h] Francesco Pineider,[ij] Claudio Sangregorio[j] and Alessandro Lascialfari[fg]

Received 5th March 2013
Accepted 14th April 2013

DOI: 10.1039/c3nr01119d

www.rsc.org/nanoscale

We describe an environmentally friendly, top-down approach to the synthesis of $Au_{89}Fe_{11}$ nanoparticles (NPs). The plasmonic response of the gold moiety and the magnetism of the iron moiety coexist in the $Au_{89}Fe_{11}$ nanoalloy with strong modification compared to single element NPs, revealing a non-linear surface plasmon resonance dependence on the iron fraction and a transition from paramagnetic to a spin-glass state at low temperature. These nanoalloys are accessible to conjugation with thiolated molecules and they are promising contrast agents for magnetic resonance imaging.

Introduction

Extraordinary physical–chemical properties are found in nanoscale gold[1,2] and iron.[3–5] Gold nanoparticles (AuNPs) have surface plasmon resonances in the visible range[2,6] and they are biocompatible,[7] chemically inert[1] and easily functionalizable through the formation of sulfur–gold bonds.[1,8] Iron nanoparticles (FeNPs) have high saturation magnetization[9] and they are biocompatible,[10] although they easily undergo oxidation in the absence of efficient passivation coatings[3] and their surface functionalization can be complex.[10]

Combining the physical–chemical properties of gold and iron in a single nanostructure would be useful in various applications,[11] such as in nanomedicine,[12,13] information technology[14–17] and catalysis.[18–20] In particular for what concern Au–Fe alloys, the high spin–orbit coupling characteristics of Au may induce appealing properties for spintronic applications, like high magnetic anisotropy,[21] large magneto-optical responses,[22] high magneto-resistance[23–25] and spin Hall effects.[26,27]

Au–Fe alloys with an Fe content exceeding 2.5% are not thermodynamically stable at room temperature,[28] although kinetically stable bulk AuFe alloys can be obtained by quick cooling of the melted metals[29,30] and thin alloy films can be obtained by radiofrequency sputtering.[22] At the nanoscale, the attempts to synthesize gold–iron alloy nanoparticles on substrates or in solution have been limited so far. AuFe alloy nanoparticles (AuFeNPs) were obtained by sequential ion implantation of iron in AuNPs embedded in a silica matrix,[15,31,32] by simultaneous reduction of Au salts and decomposition of Fe compounds in the presence of capping molecules dissolved in liquid solutions,[33–42] by electrodeposition on amorphous carbon electrodes from an aqueous solution of electrolytes,[43] in high-vacuum chambers by pulsed laser deposition[44,45] or by evaporation of a bulk alloy on a liquid hydrocarbon substrate.[46]

Reports on structure–property relationships of these nanoparticles have produced conflicting information, particularly regarding their plasmonic and magnetic responses. For instance, both blue-[31,45] and red-shifted[34,35,39,40] plasmon resonances, compared to that of pure gold nanoparticles, were assigned to AuFe alloys with the same stoichiometry. Indeed, the characterizations of alloys were not accurate enough to exclude phase segregation or to confirm homogeneous alloying at the single nanoparticle level.[31,34,35,39,40,45] This is a relevant

[a]*Department of Chemical Sciences, Università di Padova, via Marzolo 1, I-35131 Padova, Italy. E-mail: vincenzo.amendola@unipd.it*

[b]*Solar & Photovoltaics Engineering Research Center, Division of Physical Sciences and Engineering, King Abdullah University of Science and Technology (KAUST), Thuwal, 23955-6900 Saudi Arabia*

[c]*Department of Molecular Sciences and Nanosystems, Università Ca' Foscari Venezia and INSTM UdR Venezia, via Torino 155/b, I-30172 Venezia-Mestre, Italy*

[d]*Advanced Nanofabrication, Imaging, and Characterization CoreLab, King Abdullah University of Science & Technology (KAUST), Thuwal 23955-6900, Saudi Arabia*

[e]*CNR – IENI, Corso Stati Uniti, 4 35127 Padova, Italy*

[f]*Dipartimento di Fisica, Università degli Studi di Milano and Consorzio INSTM, Via Celoria 16, Milano, Italy*

[g]*Dipartimento di Fisica, Università degli Studi di Pavia and Consorzio INSTM, Via Bassi 6, I-27100 Pavia, Italy*

[h]*CNR-ISTM Milano and INSTM, via C. Golgi 19, 20133 Milano, Italy*

[i]*C.N.R.-I.S.T.M. c/o Department of Chemical Sciences, Università di Padova, via Marzolo 1, I-35131 Padova, Italy*

[j]*Department of Chemistry, Università di Firenze & I.N.S.T.M., Via della Lastruccia 3, I-50019 Sesto Fiorentino (FI), Italy*

† Electronic supplementary information (ESI) available: TEM images, size histogram, HRTEM images and EFTEM mapping of PEG–AuFeNPs; temperature dependence of χ''; calibration curve for analysis of XRD data. See DOI: 10.1039/c3nr01119d

point, since bottom-up synthetic approaches often yield byproducts such as clustered iron atoms in the gold matrix,[36–40,47] iron–gold core–shell structures[11,34,35] or iron oxide–gold heterostructures and agglomerates,[39–41,44] owing to the unfavorable thermodynamics in the formation of Au–Fe alloys.[28] Moreover, the AuFeNPs obtained by all previous methods were found to have problems related to surface accessibility,[15,31–46] which is important to catalytic applications[18–20] and for conjugation with functional molecules.[11–13] Thus, new low-cost and non-toxic synthetic methods that allow the synthesis of large amounts of well-dispersed and accessible nanoparticles avoiding the thermodynamic limitations to alloy formation are needed.

Here, we describe a new environmentally friendly top-down approach for the synthesis of AuFeNPs whose surfaces are accessible to conjugation with thiolated molecules. Our AuFeNPs are composed of 89% Au and 11% Fe and they display coexisting plasmonic and magnetic properties, although with important differences compared to the single element Au or Fe nanoparticles.

Synthesis and structural characterization

We obtained the AuFeNPs by laser ablation synthesis in solution (LASiS), focusing 1064 nm laser pulses (9 ns, 10 Hz, 30 mJ per pulse) on a bulk $Au_{73}Fe_{27}$ alloy target dipped in a solution of pure ethanol (Fig. 1A). Using this top-down approach,[48–52] we were able to overcome the thermodynamic limitations to the room-temperature formation of Au–Fe alloys.[48,53] The formation of nanoparticles was immediately visible from the reddish color of the solution, which became purple after a few hours due to particle aggregation. After LASiS, an aqueous solution containing disodium ethylenediaminetetraacetic acid (EDTA) and thiolated polyethyleneglycol (PEG) was added to the AuFeNP dispersion in ethanol and the solution was kept at 60 °C for 1 hour (Fig. 1B). A few minutes after the addition of EDTA–PEG, the color of the solution changed back from purple to reddish. The AuFeNP solution was then purified by dialysis and washed multiple times with deionized water. The final solution of PEG–AuFeNPs was indefinitely stable in water and air over time.

We used powder X-ray diffraction (XRD) analysis to identify the crystalline phase of the PEG–AuFeNPs. The diffraction pattern showed a face-centered cubic structure (fcc) analogous to pure gold (Fig. 1C). There were no peaks of other iron compounds like iron oxides or metal iron in the diffraction pattern of PEG–AuFeNPs. The refined lattice parameter of the fcc unit cell was 0.4041 nm, smaller than that of pure gold (0.4079 nm, see ESI†). This is compatible with an alloy of Fe and Au where iron atoms are present in the Au crystal lattice as random substitutional impurities[28,30] therefore the PEG–AuFeNPs are a solid solution of Au and Fe. To determine the iron content in the AuFeNPs, we compared the experimentally measured refined lattice parameter with those reported for bulk AuFe in the literature (for details see Materials and methods), and we found that it corresponds to an alloy with 89% Au and 11% Fe elemental composition. We found exactly the same elemental composition of $Au_{89}Fe_{11}$ by inductively coupled plasma-mass spectrometry (ICP-MS).

The iron content in our PEG–AuFeNPs is lower than in the bulk $Au_{73}Fe_{27}$ alloy target used for LASiS, suggesting that iron was lost during the laser ablation process. In LASiS, a difference between the stoichiometry of alloy nanoparticles and the original alloy target is observed when the two elements in the alloy have different reactivities or different vaporization heats.[48,53,54] Here, the vaporization heats of gold and iron are similar (324 and 340 kJ mol^{-1}, respectively), but iron can react with oxygen that is dissolved in non-deaerated solvents, as reported for instance during LASiS of NiFe NPs.[55] Transmission electron

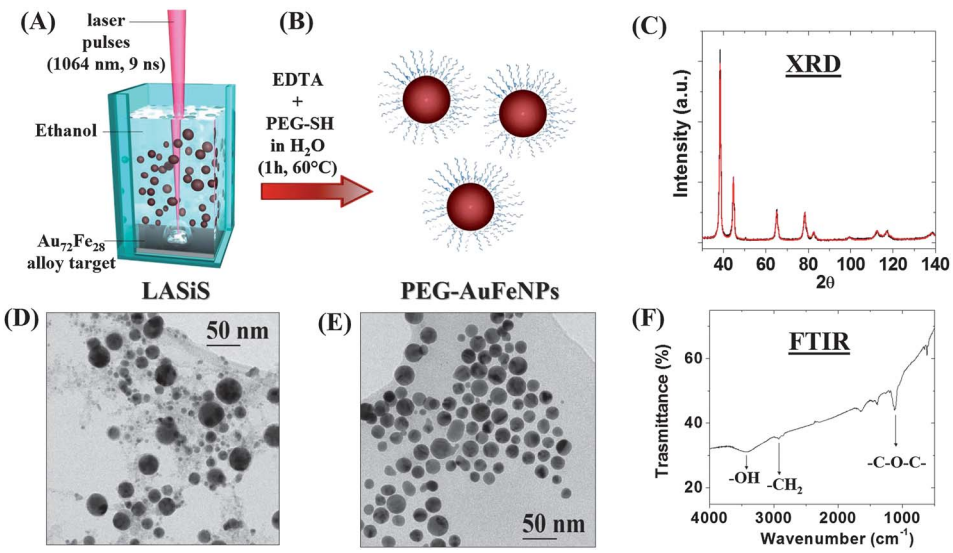

Fig. 1 Synthesis and characterization of PEG–AuFeNPs. (A) Water-soluble PEG–AuFeNPs were obtained in two steps: in the first step, AuFeNPs were produced in ethanol from a $Au_{72}Fe_{28}$ bulk target by LASiS; (B) in the second step, the NPs were treated with EDTA and conjugated with thiolated PEG to obtain PEG–AuFeNPs that were stable in water. (C) Powder XRD analysis of PEG–AuFeNPs (black line) and Rietveld fitting (red line). (D–E) TEM images of AuFeNPs as obtained by LASiS in EtOH (D) and after treatment with EDTA and coating with PEG (E). (F) The FTIR spectrum collected from the PEG–AuFeNP powder indicating the vibrational fingerprint of PEG.

microscopy (TEM) images of the AuFeNP solution just after LASiS but prior to the addition of EDTA/PEG indicated the presence of iron oxide and amorphous phases (Fig. 1D and S1A in the ESI†), likely due to the reaction of ablated Fe atoms with the liquid solution. A similar result was reported for laser ablation of bulk iron in various solvents such as ethanol and water.[56–58] The addition of EDTA and subsequent dialysis were required for selective removal of iron oxides and hydroxides,[56,57] without affecting the phase of alloy AuFeNPs. The TEM images of the PEG–AuFeNP solution indicate that all the iron oxide and amorphous phases were effectively removed by the EDTA and dialysis steps (Fig. 1E and S1B in the ESI†), which is in agreement with the XRD results. Indeed, the surfaces of the AuFeNPs obtained following this procedure were free from other stabilizing molecules and highly available for conjugation with thiolated molecules, exploiting the formation of stable Au–S bonds with gold atoms on the surfaces. Hence, we added thiolated PEG simultaneously with EDTA to coat the AuFeNPs with a shell of hydrophilic polymer. The successful coating of AuFeNPs with PEG, after the purification/washing stages, was confirmed by Fourier transform infrared (FTIR) spectroscopy of a dried sample (Fig. 1F). This one-pot surface conjugation of AuFeNPs with the desired thiolated molecules is highly important in most technological applications[11–13] and in the accurate characterization of the magnetic and plasmonic properties of well-dispersed (*i.e.*, not agglomerated) alloy nanoparticles.

The TEM results indicate that PEG–AuFeNPs have an average size of 30 nm, with 90% of particles comprised in the 15–40 nm range (see the size histogram in Fig. S1C in the ESI†) and they have well-defined crystalline structures. We observed also stacking faults and twinned crystallites in the nanoalloys (Fig. S1D and E in the ESI†). Planar defects in fcc metals are usually associated with internal stresses due to rapid cooling,[59] and are typical of LASiS.[48,53] We used energy-filtered TEM (EFTEM) to gather additional information on the elemental distribution of Au and Fe in individual PEG–AuFeNPs. We performed elemental mapping on five nanoparticles with sizes between 15 and 50 nm by selecting the Au N-edge (83 eV) and the Fe L-edge (708 eV) respectively (Fig. 2A and S2 in the ESI†). In all particles analyzed, we observed a complete overlap of the distribution of gold and iron, suggesting that the particles had a homogeneous alloy structure. Moreover, we found that the percentage of Fe in each single nanoparticle oscillated between 15% and 9%, with an average value of 11%, which is in fair agreement with the XRD and ICP-MS evaluations. We further confirmed the homogeneous distribution of Fe in the nanoalloy using X-ray energy dispersive spectroscopy (XEDS) within one single nanoparticle with a spatial resolution of 1 nm, performed in the scanning transmission electron microscopy (STEM) configuration (Fig. 2B).

Remarkably, the results of all structural characterizations were the same regardless of the different PEG–AuFeNP synthetic batches and of the amount of time elapsed after synthesis, which demonstrates the reproducibility of the synthetic method and the stability over time of our nanoalloys in air and water.

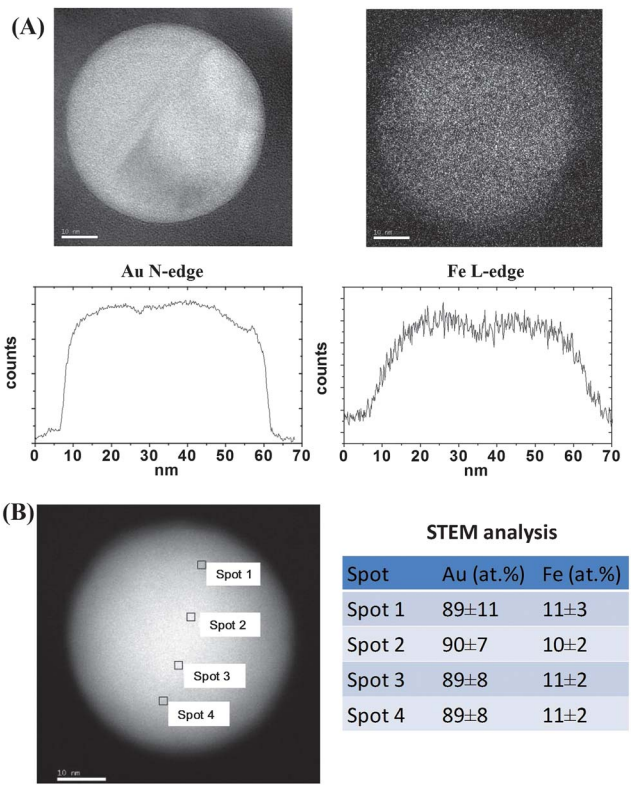

STEM analysis

Spot	Au (at.%)	Fe (at.%)
Spot 1	89±11	11±3
Spot 2	90±7	10±2
Spot 3	89±8	11±2
Spot 4	89±8	11±2

Fig. 2 Single nanoparticle elemental analysis. (A) EFTEM mapping of an Au N-edge (83 eV) and a Fe L-edge (708 eV), showing that both elements overlapped. The scale bars are 10 nm. (B) STEM analysis carried out on a single AuFeNP to assess the phase homogeneity and the $Au_{89}Fe_{11}$ stoichiometry of the nanoalloy. The scale bar is 10 nm.

Optical properties

The UV-visible absorption spectra of AuFeNPs in ethanol (as obtained from LASiS) and of PEG–AuFeNPs in water both indicated the presence of surface plasmon resonance (Fig. 3A). Surface plasmon bands originate from the collective excitation of conduction electrons in nanoscale metals by annihilation of

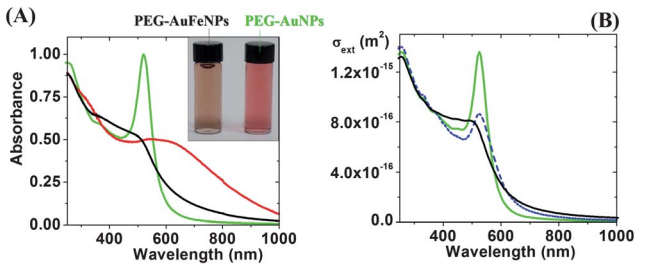

Fig. 3 Optical properties of AuFeNPs. (A) UV-vis spectra of AuFeNPs as obtained by LASiS in ethanol (red line), of PEG–AuFeNPs in water (black line) and of PEG-coated AuNPs (green line). Inset: PEG–AuFeNPs in water are reddish in color (left), different from the purple color of pure AuNPs (shown on the right for comparison). (B) The extinction cross-section (σ_{ext}) calculated using the Mie model for 30 nm $Au_{89}Fe_{11}$ (black line) and Au (green line) nanospheres in water. The dashed blue line is the σ_{ext} calculated using the Mie model for a 30 nm nanosphere with an optical constant obtained by the linear weighted average of pure Au and Fe metals (for details, see text).

the incident photons,[60] and their resonance energy depends on the composition, shape and aggregation of the NPs as well as on their chemical–physical environment.[60–62] In the case of AuFeNPs in ethanol, the plasmon band extended from 500 nm to 700 nm due to aggregation of particles and consequent plasmon hybridization (red line in Fig. 3A),[62,63] while in the case of PEG–AuFeNPs, a narrower plasmon resonance was centered at 510 nm (black line in Fig. 3A), suggesting that the NPs were well dispersed and isolated in the liquid.[63] For comparison, the plasmon band of pure PEG–AuNPs with the same average size dispersed in H_2O is also shown in Fig. 3A. The plasmon band of PEG–AuFeNPs is less intense and blue-shifted by 10 nm compared with the plasmon band of PEG–AuNPs. The Mie model provides a good description of the optical properties of nanospheres, when the appropriate optical constant is used.[60,63] We therefore obtained the optical constant of an $Au_{89}Fe_{11}$ alloy by the weighted average of the optical constants of pure gold and of an alloy with composition as close as possible to our particles among those available in the literature, *i.e.* of a bulk $Au_{84}Fe_{16}$ alloy (measured by ellipsometry),[22] and thus we calculated the extinction spectrum of a 30 nm metal sphere by the Mie model. As shown in Fig. 3B, the calculated spectrum (black line) agrees well with the experimental one, reproducing both damping and the blue shift of the surface plasmon resonance. This result also suggests that previous reports on red-shifted plasmon resonance in Au–Fe alloy nanoparticles[34,35,39,40,64] are likely due to samples with heterogeneous composition or to particle aggregation.

As shown in Fig. 3A, the plasmon band is damped by the presence of Fe atoms in the gold lattice, which was somewhat expected because metal FeNPs do not have a plasmon resonance in the visible range.[60] However, it is worth noting that much lower plasmon damping is found in the extinction spectrum of 30 nm $Au_{89}Fe_{11}$NPs calculated by considering as the optical constant (ε_{Alloy}) the linear average of the optical constants of pure Au (ε_{Au}) and Fe (ε_{Fe}), *i.e.*, $\varepsilon_{Alloy} = 0.89\varepsilon_{Au} + 0.11\varepsilon_{Fe}$ (dashed line in Fig. 3B), instead of using the experimental optical constant for the $Au_{84}Fe_{16}$ alloy reported in ref. 22. Also the experimentally observed blue shift of the plasmon resonance is not reproduced by the blue dashed curve in Fig. 3B. This result indicates that plasmon damping in AuFe nanoalloys has a non-linear dependence on the iron fraction that can be accounted only by the appropriate choice of the optical constant in the spectral range of the plasmon resonance. Indeed, the nanoalloy extinction spectrum differs from that of pure AuNPs in the range below 450 nm (Fig. 3A and B). According to previous reports on thin AuFe alloy films,[22] such differences are due to single electron transitions from iron d states lying below the Fermi surface of the $Au_{89}Fe_{11}$ nanoalloy. Low-frequency interband transitions are frequently observed in alloys of noble metals and transition metals with partially occupied d states[65–67] and they are known to strongly affect the intensity of the plasmon resonance by introducing an additional term to the effective free electron relaxation rate, because plasmon excitations can rapidly decay into electron–hole pairs.[65] The nonlinear dependence of the plasmon damping in relation to the concentration of Fe is therefore likely related to the effect of iron d states on the relaxation frequency of the conduction electrons[22,65,67,68] and this finding further supports the formation of an alloy in which the Fe is homogeneously dispersed in the crystal lattice.

Magnetic properties

The magnetic properties of the $Au_{89}Fe_{11}$ nanoalloy retain the main features of Au–Fe solid solutions. We measured the magnetic field dependence of the magnetization (M) of PEG–AuFeNPs at two different temperatures. At 300 K, M linearly increased with the applied field (blue curve in Fig. 4A) as expected for a system made of paramagnetic impurities (Fe) dispersed in a diamagnetic host (gold).[69] Conversely, at low temperature (3 K), the signature of collective magnetic correlations appeared, as suggested by the magnetic irreversibility we observed on cycling the magnetic field between ± 5 T (blue line, Fig. 4A). At the lowest measuring field of -5 T, the hysteresis loop was open with a coercive field, $\mu_0 H_C = 121$ mT, and reduced remnant magnetization, $M_{0T}/M_{5T} = 0.30$; at the highest measuring field of 5 T, M reached 9.9 A m^2 kg^{-1}, a value 5 times larger than at 300 K, although still far from saturation.

The temperature dependence of M was measured also using a smaller probe field (5 mT) after the Zero Field Cooled (ZFC) and Field Cooled (FC) procedures (Fig. 4B), and displayed the thermal irreversibility typical of a spin freezing process. The ZFC magnetization exhibited a broad maximum centred at 75 K, while the FC magnetization decreased from 3 K to 15 K and then followed the same trend of the ZFC curve, approaching $T > 100$ K. We further investigated the nature of this spin "blocking" by

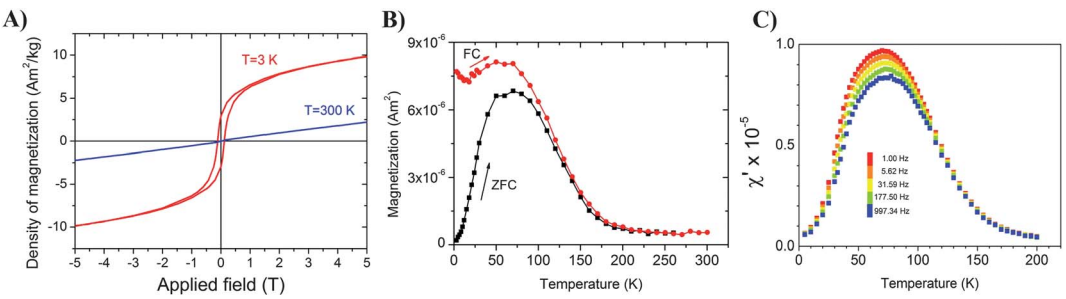

Fig. 4 Magnetic properties of AuFeNPs. (A) Hysteresis loops measured at 3 K and 300 K. (B) Temperature dependence of the ZFC and FC magnetizations. (C) The in-phase component, χ', of the AC magnetic susceptibility recorded at frequencies between 1 Hz and 1000 Hz.

measuring the temperature dependence of the AC magnetic susceptibility, $\chi = \chi' + i\chi''$, in the 1 Hz to 1 kHz frequency range. Below *ca.* 130 K, the in-phase component, χ', had a frequency-dependent signal with a broad maximum, which shifted from 70.6 K to 74.6 K when the frequency was increased by three orders of magnitude (Fig. 4C). The development of the frequency dependence was accompanied by a non-zero, out-of-phase component, χ'', which increased as the temperature decreased to *ca.* 50 K (see Fig. S3 in the ESI†). A rough indication of the nature of the observed magnetic dynamics can be obtained by considering the shift at which χ' is maximum (T_{max}) with a decade change in frequency and applying the empirical formula proposed by Mydosh and Barrett.[70] In this way, we found that $\Delta T_{max}/[T_{max}\Delta\log(2\pi\nu)] \sim 0.01$–$0.02$, which is in the range expected for canonical spin-glass systems (10^{-3} to 10^{-2}).[70]

Disordered bulk $Au_{1-x}Fe_x$ alloys with their iron content below the percolation threshold ($x = 0.155$) exhibit a paramagnetic to spin-glass transition at a freezing temperature, T_g, which increases with x up to *ca.* 50 K.[71] The spin-glass behavior originates from the random distribution of the Fe atoms within the gold lattice and competing ferromagnetic (FM)–antiferromagnetic (AFM) exchange interactions between Fe through the conduction band of Au (the Ruderman–Kittle–Kasuya–Yosida mechanism).[72–74] In contrast, by increasing the concentration above the percolation threshold, Fe atoms start to cluster, and the nearest-neighbor direct exchange leads to a long-range ferromagnetic order. When the iron content exceeds 24%, a transition to a ferromagnetic-ordered state occurs, while in the intermediate composition range (from 16% to 24%), an additional transition below the critical temperature from the ferromagnetic to the spin-glass state is observed (the re-entrant spin-glass state).[71]

It is noteworthy that the value of the density of magnetization (9.9 A m^2 kg^{-1}) measured at 5 T, which corresponds to a magnetic moment of $0.32\mu_B$ per atom. Assuming that only Fe atoms contribute to the total magnetization, the net magnetization of Fe is 292 ± 30 A m^2 kg^{-1}, which corresponds to a magnetic moment of $2.92 \pm 0.3\mu_B$ per Fe atom. This value is remarkably high if compared to the bulk Fe body-centered cubic structure (bcc) ($2.2\mu_B$ per Fe atom),[3] particularly if we consider that the system is still far from saturation. However, it is in good agreement with experimental values[75] and theoretical predictions[76] reported for the bulk Au–Fe alloy, where the Fe atoms in the fcc crystalline structure are in the high spin state due to the stabilizing effect conferred by the lattice expansion.[77] On the other hand, also the magnetic polarization of Au atoms by the nearest-neighbor Fe atoms provides an additional contribution to the total magnetic moment,[75] but it is usually found to be lower than $0.03\mu_B$ per Au atom and, therefore, it does not produce a significant variation of M.[78] Both the low-temperature spin-glass behavior and the large net magnetization of Fe fully support the observation of the homogenous random distribution of iron atoms within each nanoalloy particle and exclude the presence of clustered Fe centres.

Relaxivity properties

Since the PEG–AuFeNPs are paramagnetic at room temperature, we evaluated their ability to act as contrast agents in magnetic resonance imaging. The ^{1}H NMR dispersion profile was measured at room temperature in the frequency range 10 kHz ≤ ν ≤ 60 MHz.[79] This range was chosen to cover the typical fields in MRI tomographs, used in both clinical (H = 0.2, 0.5 and 1.5 T) and research laboratory settings. The relaxivities r_1 and r_2 weighted by the magnetic center concentration (*i.e.*, the inverse of transverse ^{1}H nuclear relaxation times T_1 and T_2, respectively) as a function of frequency are shown in Fig. 5A. From the $r_1(\nu)$ behavior, we gather information on the physical mechanisms affording the shortening of ^{1}H nuclear relaxation times. In general, two different relaxation mechanisms contribute to the $r_1(\nu)$ curve.[80–82] At low frequencies (≤1–5 MHz), the mechanism driving the nuclear relaxation is the Néel relaxation of the particle magnetization, giving a correlation time related to the magnetic anisotropy barrier;[80–82] at high frequencies (≥1–10 MHz), the dominant mechanism is the Curie relaxation, which takes into account the diffusion of water molecules (with a diffusion correlation time $\tau_D = r^2/D$, where r is the distance of the closest approach and D the diffusion coefficient of water molecules) in the presence of magnetic centers.[80–82] While the first mechanism gives a flattening of $r_1(\nu)$ at frequencies ν < 1–5 MHz, the second mechanism is responsible for the maximum in $r_1(\nu)$ at higher frequencies. In addition, for particles characterized by a distance of <5 nm between the magnetic core and the hydrogen nuclei of the bulk water, a dispersion at intermediate frequencies occurs.[80–82] In PEG–AuFeNPs, both the high-frequency maximum and the low-frequency dispersion are absent in the $r_1(\nu)$ plot (Fig. 5A). This can be attributed to the

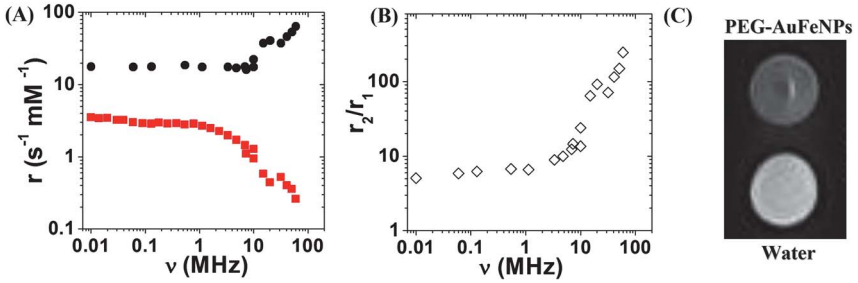

Fig. 5 Relaxivity properties of AuFeNP solutions. (A) Longitudinal (r_1) and transversal (r_2) relaxation rates for PEG–AuFeNPs (red squares and black circles, respectively). (B) r_2/r_1 ratio *vs.* frequency. (C) Even at a low frequency (8.5 MHz), the phantom containing a solution of the nanoalloy is darker than pure water, showing the contrast ability of the PEG–AuFeNP solution.

dominant contribution coming from the high magnetic anisotropy[83,84] due to the diameter of about 30 nm of PEG–AuFeNPs and to the PEG shell, the thickness of which in water can be estimated to be 10–15 nm.[85]

Instead, $r_2(\nu)$ rapidly increases up to 64 s^{-1} mM^{-1} for $\nu >$ 7 MHz (Fig. 5A), *i.e.*, up to a relaxivity comparable to commercial superparamagnetic contrast agents like Endorem™ (99 s^{-1} mM^{-1}) for a typical clinical field $H = 1.5$ T. Therefore, AuFe nanoalloys are promising negative contrast agents, as also confirmed by the efficiency parameter r_2/r_1, reported in Fig. 5B, that is greater than 5 in all frequency ranges and reaches values above 10^2 at high fields, whereas the threshold value is about 2 for most negative contrast agents.[82–84] An example for the contrast ability of the PEG–AuFeNPs is obtained by comparing a phantom containing the aqueous suspension of PEG–AuFeNPs with a phantom containing pure water. The T_2-weighted image, reported in Fig. 5C, is obtained with a Spin Echo sequence and it is in agreement with the measured r_2 relaxivities at 8.5 MHz (operating field of 0.2 T). As can be seen from the image, the solution containing the AuFe nanoalloy is darker than water, confirming the efficacy of our material in contrasting images.

Conclusions

In summary, we found that plasmonic and magnetic properties coexist in $Au_{89}Fe_{11}$ nanoalloys obtained by laser ablation synthesis in solution. LASiS is a top-down "green" technique capable of overcoming the thermodynamic limitations for the synthesis of Au–Fe alloys and generating nanoparticles that can be coated in one-pot with thiolated ligands. The as-obtained PEG-coated nanoalloys have homogeneous $Au_{89}Fe_{11}$ composition and excellent stability in air and in aqueous solutions. The ability of PEG–AuFeNPs to act as negative contrast agents for magnetic resonance imaging is also demonstrated. The investigation of plasmonic properties revealed a nonlinear dependence on the composition. Most importantly, plasmonic and magnetic properties coexist in the nanoalloy, suggesting the possibility that novel spin-dependent plasmonic phenomena might be observed at the nanoscale. Our results mark a step forward in the development of a new class of multifunctional nanoalloys with potential applications in nanomedicine, photonics, spintronics and magneto-plasmonic devices.

Materials and methods

AuFeNP synthesis and PEGylation

AuFeNPs were obtained by laser ablation synthesis in solution (LASiS). Laser ablation was carried out with Nd:YAG Quantel YG981E laser pulses at 1064 nm (9 ns) focused with a f 10 cm lens on a metal plate placed at the bottom of a cell containing pure ethanol (HPLC grade, Fluka). Pulses of 30 J cm^{-2} at a 10 Hz repetition rate and a plate of AuFe alloy (Au 73% atomic, Fe 27% atomic, 99.9% purity, purchased from MaTecK GmbH) were used for LASiS of AuFeNPs. Scanning Electron Microscopy-Energy Dispersive Spectroscopy analysis with a FEI Quanta 200 was performed on the target prior to LASiS to assess the uniformity of the alloy plate.

After the LASiS, the ethanol solutions of AuFeNPs (0.05 mg ml^{-1}) were diluted to a ratio of 1 : 2 with an aqueous solution of 5.0 mM disodium ethylenediaminetetraacetate (EDTA >98%, Sigma Aldrich) and thiolated 0.05 mM polyethylene glycol (PEG–SH, 5000 M_w, from Lysan Bio). The solution was kept at 60 °C for 1 hour and then washed with dialysis concentration membranes by multiple washing cycles with deionized water at 2000 rcf (10 000 Da, Vivaspin from Sartorius) and finally resuspended in deionized water.

AuFeNP structural characterization

UV-vis absorption spectra were recorded with a Varian Cary 5 spectrometer using 2 mm optical path quartz cells. FTIR measurements were carried out on a dried PEG–AuFeNP powder on a KBr window with a Nicolet 5700 spectrophotometer.

The inductively coupled plasma-mass spectrometry (ICP-MS) measurements were carried out with a Thermo Elemental X7 Series instrument equipped with the PlasmaLab software package. For instrument calibration, standard Au and Fe solutions were purchased from Spectrascan.

The X-ray diffraction pattern was collected by a Philips diffractometer constituted by an X'Pert vertical goniometer with Bragg–Brentano geometry, a focusing graphite monochromator and a proportional counter with a pulse-height discriminator. Nickel-filtered Cu Kα radiation and a step-by-step technique were employed (steps of $2\theta = 0.05°$), with collection times of 30 s per step. A previously published method was used for line broadening analysis (LBA).[86] The quantitative phase analysis by X-ray diffraction was performed using the Rietveld method (DBWS9600 computer program written by Sakthivel and Young and modified by Riello *et al.*).[86] To take into account $Au_{1-x}Fe_x$ solid solutions with different structures (bcc and fcc), the calibration was obtained by fitting the average volume per atom in the cell. The calibration curve and the equation of the polynomial interpolation are reported in Fig. S4.†

Transmission electron microscopy analysis was performed with a JEOL JEM 3010 microscope operating at 300 kV and equipped with a Gatan Multiscan CCD Camera model 794. The samples for TEM analysis were prepared by evaporating NP suspensions on a copper grid coated with an amorphous carbon holey film.

Additional TEM analysis was carried out with a Titan™ TEM (FEI Company, Hillsboro, OR 97124) operating at 300 keV beam energy and equipped with a Tridiem™ post-column energy filter (Gatan, Inc., Pleasanton, CA 94588) and an X-ray energy dispersive spectroscopy (XEDS) system (EDAX Inc., Mahwah, NJ 07430). The samples were imaged at a magnification of 500 k× in energy-filtered TEM (EFTEM) mode with a 14 eV energy slit inserted around the zero energy-loss electrons for acquiring the high-resolution TEM (HRTEM) micrographs. The presence of peaks in the processed Fast Fourier Transforms (FFTs) of each HRTEM image showed that all of the nanoparticles investigated had a crystalline structure. The HRTEM images were acquired close to 1–2 Scherzer defocus. Elemental mapping of Au and Fe was performed by selecting their N-edge (83 eV) and L-edge (708 eV), respectively, for the three-window mapping method (1 post-edge

of 15 eV and 2 pre-edge with 15 eV width). Each elemental map was then line profiled across the diameter of each nanoparticle to show the amount of elemental signal across the whole nanoparticle. Au and Fe signal counts were then summed and corrected with cross-sections using the experimental collection angle and energy windows adapted for EFTEM mapping of each element. Scanning transmission electron microscopy (STEM) was performed with the electron beam at 300 keV to acquire the X-ray energy dispersive spectra (XEDS) from different locations on the same nanoparticle with about one nanometer spatial resolution. An annular dark-field (HAADF) STEM detector from Fischione Inc. was employed to generate the STEM micrographs. Au and Fe elemental compositions were determined under standardless and Cliff–Lorimer approximations.

The sample for analysis with the Titan TEM was obtained by mixing 10 μl of PEG–AuFeNPs solution with 100 μl of a 10 mg ml^{-1} polyvinyl alcohol solution in water (PVA, average 200 000 M_w, from Fluka) and depositing one drop on a copper grid coated with a holey carbon film. PVA prevented particle agglomeration after drying the drop.

Mie model calculations

The extinction cross-section of spherical nanoparticles was calculated using the Mie model for compact spheres:[60]

$$\sigma = \frac{2\pi}{\left|\bar{k}^2\right|}\sum_{L=1}^{\infty}(2L+1)\mathrm{Re}[a_L + b_L] \quad (1a)$$

$$a_L = \frac{m\cdot\psi_L(mx)\cdot\psi_L{}'(x) - \psi_L{}'(mx)\cdot\psi_L(x)}{m\cdot\psi_L(mx)\cdot\eta_L{}'(x) - \psi_L{}'(mx)\cdot\eta_L(x)} \quad (1b)$$

$$b_L = \frac{\psi_L(mx)\cdot\psi_L{}'(x) - m\psi_L{}'(mx)\cdot\psi_L(x)}{\psi_L(mx)\cdot\eta_L{}'(x) - m\psi_L{}'(mx)\cdot\eta_L(x)} \quad (1c)$$

$$m = \frac{n(R)}{n_m} \quad (1d)$$

$$x = |\bar{k}|R, \quad (1e)$$

where σ is the extinction cross-section of a sphere of radius R, k is the incident photon wavevector, ψ_L and η_L are the spherical Riccati–Bessel functions, n_m is the real refraction index of the non-absorbing surrounding medium, and $n(R)$ is the complex refractive index of the sphere of radius R. In all calculations, we set the multipolar order to $L = 3$ and $n_m = 1.334$ (for water matrix).

Because the optical constants of the $Au_{89}Fe_{11}$ alloy are not available in the literature, we use the linear averaging of the optical constants of pure Au from ref. 87 and for $Au_{84}Fe_{16}$ from ref. 22. The optical constants are corrected for size, as reported previously,[60,63] although the corrections have negligible effects on 30 nm nanoparticles, which fall between the intrinsic and extrinsic size effect regimes.[60]

Magnetic characterization

Magnetic measurements were performed using a Quantum Design MPMS SQUID magnetometer operating in the 1.8–350 K temperature range with the applied field up to 5.0 T. These measurements were carried out on aqueous solution placed in a gel-cap and on dried powder obtained by gentle evaporation of a few drops of the solution on a Teflon ribbon. The temperature dependence of the in-phase (χ') and out-of-phase (χ'') components of the AC susceptibility was measured with the same apparatus on a powder sample in the 1–1000 Hz frequency range with a field amplitude of 240 A m^{-1}. All data were corrected for the diamagnetic contribution of the sample holder and, when present, of the solvent, which were measured separately. After subtraction of the diamagnetic contributions, no noticeable differences among the magnetic behaviors of the NPs in solution and in dried powder were observed.

Relaxivity measurements

NMR data were collected by using two different pulsed FT-NMR spectrometers: (i) a Smartracer Stelar relaxometer (with the use of the Fast-Field-Cycling technique) for frequencies in the range 10 kHz $\leq \nu \leq$ 10 MHz, and (ii) a Stelar Spinmaster for $\nu >$ 10 MHz.

Standard radio frequency excitation pulse sequences, CPMG-(T2) and saturation-recovery (T1), were used. The contrast ability of PEG–AuFeNPs was investigated by measuring the longitudinal (r_1) and transversal (r_2) relaxation rates (Fig. 5A) of protons (^1H) defined as:[82]

$$r_i = [(1/T_i)_{meas} - (1/T_i)_{dia}]/c,\ i = 1, 2$$

where $(1/T_i)_{meas}$ is the value measured for a concentration c of the magnetic center (in mM^{-1}) and $(1/T_i)_{dia}$ is the nuclear relaxation rate of the diamagnetic solvent (*i.e.*, ultrapure H_2O), which is of the order of a few seconds.

MRI experiments were performed at 8.5 MHz using an Artoscan Imager by Esaote SpA (Esaote, Genova, Italy). The pulse sequence was a high-resolution spin echo sequence with TR/TE/NEX = 5000 ms/120 ms/2, matrix = 256 × 192, field of view = 180 × 180, where TE is the echo time, TR the repetition time, and NEX is the number of averages.

Acknowledgements

This research was supported by the University of Padova grant (PRAT) no. CPDA114097/11. CJF, CS, FP, AL and PA acknowledge Fondazione Cariplo (Project no. 2010-0612) and Italian MIUR (FIRB Project "RINAME" No. RBAP114AMK). FP acknowledges "Rete ItalNanoNet" (Pr. no. RBPR05JH2P).

References

1 M. C. Daniel and D. Astruc, *Chem. Rev.*, 2004, **104**, 293–346.
2 S. Eustis and M. A. El-Sayed, *Chem. Soc. Rev.*, 2006, **35**, 209–217.
3 D. L. Huber, *Small*, 2005, **1**, 482–501.
4 X. Li, D. W. Elliott and W. Zhang, *Crit. Rev. Solid State Mater. Sci.*, 2006, **31**, 111–122.
5 A. H. Lu, E. L. Salabas and F. Schuth, *Angew. Chem., Int. Ed.*, 2007, **46**, 1222–1245.

6 E. Lidorikis, *J. Quant. Spectrosc. Radiat. Transfer*, 2012, **113**, 2573–2584.
7 D. A. Giljohann, D. S. Seferos, W. L. Daniel, M. D. Massich, P. C. Patel and C. A. Mirkin, *Angew. Chem., Int. Ed.*, 2010, **49**, 3280–3294.
8 A. Ghosh, S. Basak, B. H. Wunsch, R. Kumar and F. Stellacci, *Angew. Chem., Int. Ed.*, 2011, **50**, 7900–7905.
9 D. Zhang, K. Klabunde, C. Sorensen and G. Hadjipanayis, *Phys. Rev. B: Condens. Matter Mater. Phys.*, 1998, **58**, 14167.
10 E. E. Carpenter, *J. Magn. Magn. Mater.*, 2001, **225**, 17–20.
11 S. Peng, C. Lei, Y. Ren, R. E. Cook and Y. Sun, *Angew. Chem., Int. Ed.*, 2011, **50**, 3158–3163.
12 J. R. McCarthy and R. Weissleder, *Adv. Drug Delivery Rev.*, 2008, **60**, 1241–1251.
13 J. Gao, H. Gu and B. Xu, *Acc. Chem. Res.*, 2009, **42**, 1097–1107.
14 V. Belotelov, I. Akimov, M. Pohl, V. Kotov, S. Kasture, A. Vengurlekar, A. V. Gopal, D. Yakovlev, A. Zvezdin and M. Bayer, *Nat. Nanotechnol.*, 2011, **6**, 370–376.
15 L. Bogani, L. Cavigli, C. de Julián Fernández, P. Mazzoldi, G. Mattei, M. Gurioli, M. Dressel and D. Gatteschi, *Adv. Mater.*, 2010, **22**, 4054–4058.
16 P. K. Jain, Y. Xiao, R. Walsworth and A. E. Cohen, *Nano Lett.*, 2009, **9**, 1644–1650.
17 L. Wang, C. Clavero, Z. Huba, K. J. Carroll, E. E. Carpenter, D. Gu and R. A. Lukaszew, *Nano Lett.*, 2011, **11**, 1237–1240.
18 D. Wang and Y. Li, *Adv. Mater.*, 2011, **23**, 1044–1060.
19 R. Ferrando, J. Jellinek and R. L. Johnston, *Chem. Rev.*, 2008, **108**, 845–910.
20 J. F. Soulé, H. Miyamura and S. Kobayashi, *J. Am. Chem. Soc.*, 2011, **133**, 18550–18553.
21 J. T. Wang, D. S. Wang and Y. Kawazoe, *Mater. Trans.*, 2003, **44**, 1529–1534.
22 Y. Lee, Y. Kudryavtsev, V. Nemoshkalenko, R. Gontarz and J. Rhee, *Phys. Rev. B: Condens. Matter Mater. Phys.*, 2003, **67**, 104424.
23 J. Xu, B. Hickey, M. Howson, D. Greig, R. Cochrane, S. Mahon, C. Achilleos and N. Wiser, *Phys. Rev. B: Condens. Matter Mater. Phys.*, 1997, **56**, 14602.
24 P. Allia, M. Coisson, V. Selvaggini, P. Tiberto and F. Vinai, *Phys. Rev. B: Condens. Matter Mater. Phys.*, 2001, **63**, 180404.
25 B. Gorshunov, S. Kaiser, E. Zhukova, A. Prokhorov, M. Hesselberth, J. Aarts, G. Nieuwenhuys and M. Dressel, *Phys. Rev. B: Condens. Matter Mater. Phys.*, 2009, **79**, 054203.
26 F. W. Fabris, P. Pureur, J. Schaf, V. Vieira and I. Campbell, *Phys. Rev. B: Condens. Matter Mater. Phys.*, 2006, **74**, 214201.
27 I. Sugai, S. Mitani and K. Takanashi, *IEEE Trans. Magn.*, 2010, **46**, 2559–2561.
28 H. Okamoto, *Desk Handbook: Phase Diagrams for Binary Alloys*, ASM International, Ohio, 2000.
29 P. Allia, M. Coisson, G. Durin, J. Moya, V. Selvaggini, P. Tiberto and F. Vinai, *J. Appl. Phys.*, 2002, **91**, 5936–5939.
30 B. Window, *Phys. Rev. B: Solid State*, 1972, **6**, 2013.
31 C. Fernández, G. Mattei, E. Paz, R. Novak, L. Cavigli, L. Bogani, F. Palomares, P. Mazzoldi and A. Caneschi, *Nanotechnology*, 2010, **21**, 165701.
32 G. Mattei, C. de Julián Fernández, G. Battaglin, C. Maurizio, P. Mazzoldi and C. Scian, *Nucl. Instrum. Methods Phys. Res., Sect. B*, 2006, **250**, 225–228.
33 I. Chiang and D.-H. Chen, *Adv. Funct. Mater.*, 2007, **17**, 1311–1316.
34 N. Dahal, V. Chikan, J. Jasinski and V. J. Leppert, *Chem. Mater.*, 2008, **20**, 6389–6395.
35 N. Dahal, J. T. Wright, T. M. Willey, R. W. Meulenberg and V. Chikan, *ACS Appl. Mater. Interfaces*, 2010, **2**, 2238–2247.
36 A. Naitabdi and R. Cuenya, *Appl. Phys. Lett.*, 2007, **91**, 113110.
37 A. Naitabdi, L. K. Ono, F. Behafarid and B. R. Cuenya, *J. Phys. Chem. C*, 2009, **113**, 1433–1446.
38 R. Cuenya, L. K. Ono, J. R. Croy, A. Naitabdi, H. Heinrich, J. Zhao, E. E. Alp, W. Sturhahn and W. Keune, *Appl. Phys. Lett.*, 2009, **95**, 143103.
39 H. L. Liu, J. H. Wu, J. H. Min and Y. K. Kim, *J. Appl. Phys.*, 2008, **103**, 07D529.
40 H. L. Liu, P. Hou, W. X. Zhang, Y. K. Kim and J. H. Wu, *Nanotechnology*, 2010, **21**, 335602.
41 Y. Vasquez, Z. Luo and R. E. Schaak, *J. Am. Chem. Soc.*, 2008, **130**, 11866–11867.
42 A. Wijaya, K. A. Brown, J. D. Alper and K. Hamad-Schifferli, *J. Magn. Magn. Mater.*, 2007, **309**, 15–19.
43 D. Lu, K. Domen and K. Tanaka, *Langmuir*, 2002, **18**, 3226–3232.
44 V. Caps, S. Arrii, F. Morfin, G. Bergeret and J. L. Rousset, *Faraday Discuss.*, 2008, **138**, 241–256.
45 W. S. Chang, J. W. Park, V. Rawat, T. Sands and G. U. Lee, *Nanotechnology*, 2006, **17**, 5131.
46 T. Taniyama, R. Ogawa, T. Sato and E. Ohta, *Mater. Sci. Eng., A*, 1996, **217**, 319–321.
47 Z. Swiatkowska-Warkocka, K. Kawaguchi, Y. Shimizu, A. Pyatenko, H. Wang and N. Koshizaki, *Langmuir*, 2012, **28**, 4903–4907.
48 V. Amendola and M. Meneghetti, *Phys. Chem. Chem. Phys.*, 2009, **11**, 3805–3821.
49 G. Compagnini, A. A. Scalisi and O. Puglisi, *Phys. Chem. Chem. Phys.*, 2002, **4**, 2787–2791.
50 E. Messina, L. D'Urso, E. Fazio, C. Satriano, M. Donato, C. D'Andrea, O. Maragò, P. Gucciardi, G. Compagnini and F. Neri, *J. Quant. Spectrosc. Radiat. Transfer*, 2012, **113**, 2490–2498.
51 F. Mafune, J. Kohno, Y. Takeda, T. Kondow and H. Sawabe, *J. Phys. Chem. B*, 2000, **104**, 9111–9117.
52 A. Kabashin and M. Meunier, *J. Appl. Phys.*, 2003, **94**, 7941–7943.
53 V. Amendola and M. Meneghetti, *Phys. Chem. Chem. Phys.*, 2013, **15**, 3027–3046.
54 Z. Yan and D. B. Chrisey, *J. Photochem. Photobiol., C*, 2012, **13**, 204.
55 J. Jakobi, S. Petersen, A. Menéndez-Manjón, P. Wagener and S. Barcikowski, *Langmuir*, 2010, **26**, 6892–6897.
56 V. Amendola, M. Meneghetti, G. Granozzi, S. Agnoli, S. Polizzi, P. Riello, A. Boscaini, C. Anselmi, G. Fracasso and M. Colombatti, *J. Mater. Chem.*, 2011, **21**, 3803–3813.

57 V. Amendola, P. Riello, S. Polizzi, S. Fiameni, C. Innocenti, C. Sangregorio and M. Meneghetti, *J. Mater. Chem.*, 2011, **21**, 18665–18673.

58 V. Amendola, P. Riello and M. Meneghetti, *J. Phys. Chem. C*, 2011, **115**, 5140–5146.

59 R. E. Smallman and A. H. W. Ngan, *Physical Metallurgy and Advanced Materials*, Butterworth Heinemann, 2007.

60 U. Kreibig and M. Vollmer, *Optical Properties of Metal Clusters*, Springer, Berlin, 1995.

61 M. Rycenga, C. M. Cobley, J. Zeng, W. Li, C. H. Moran, Q. Zhang, D. Qin and Y. Xia, *Chem. Rev.*, 2011, **111**, 3669.

62 K. L. Kelly, E. Coronado, L. L. Zhao and G. C. Schatz, *J. Phys. Chem. B*, 2003, **107**, 668–677.

63 V. Amendola and M. Meneghetti, *J. Phys. Chem. C*, 2009, **113**, 4277–4285.

64 J. F. Bondi, R. Misra, X. Ke, I. T. Sines, P. Schiffer and R. E. Schaak, *Chem. Mater.*, 2010, **22**, 3988–3994.

65 M. G. Blaber, M. D. Arnold and M. J. Ford, *J. Phys.: Condens. Matter*, 2010, **22**, 143201.

66 H. Koike, S. Yamaguchi and T. Hanyu, *J. Phys. Soc. Jpn.*, 1976, **40**, 219–225.

67 O. Hunderi, *Solid State Commun.*, 1972, **11**, 885–888.

68 D. Beaglehole and T. J. Hendrickson, *Phys.Rev. Lett.*, 1969, **22**, 133–136.

69 V. Cannella and J. Mydosh, *Phys. Rev. B: Solid State*, 1972, **6**, 4220.

70 J. A. Mydosh and T. W. Barrett, *Spin glasses: an experimental introduction*, Taylor & Francis, London, 1993.

71 B. Verbeek and J. Mydosh, *J. Phys. F: Met. Phys.*, 2001, **8**, L109.

72 A. Chakrabarti and C. Dasgupta, *Phys. Rev. Lett.*, 1986, **56**, 1404–1407.

73 I. Campbell, S. Senoussi, F. Varret, J. Teillet and A. Hamzić, *Phys. Rev. Lett.*, 1983, **50**, 1615–1618.

74 A. Prokhorov, V. Anzin, D. Vitukhnovskiĭ, E. Zhukova, I. Spektor, B. Gorshunov, S. Vongtragool, M. B. S. Hesselberth, J. Aarts and G. Nieuwenhuys, *J. Exp. Theor. Phys.*, 2006, **103**, 887–896.

75 F. Wilhelm, P. Poulopoulos, V. Kapaklis, J. P. Kappler, N. Jaouen, A. Rogalev, A. Yaresko and C. Politis, *Phys. Rev. B: Condens. Matter Mater. Phys.*, 2008, **77**, 224414.

76 S. Khmelevskyi, J. Kudrnovský, B. Gyorffy, P. Mohn, V. Drchal and P. Weinberger, *Phys. Rev. B: Condens. Matter Mater. Phys.*, 2004, **70**, 224432.

77 V. Moruzzi, P. Marcus, K. Schwarz and P. Mohn, *Phys. Rev. B: Condens. Matter Mater. Phys.*, 1986, **34**, 1784.

78 J. Cable and E. Wollan, *Phys. Rev. B: Solid State*, 1973, **7**, 2005.

79 G. Ferrante and S. Sykora, *Adv. Inorg. Chem.*, 2005, **57**, 405–470.

80 A. Roch, R. N. Muller and P. Gillis, *J. Chem. Phys.*, 1999, **110**, 5403.

81 P. Gillis, F. Moiny and R. A. Brooks, *Magn. Reson. Med.*, 2002, **47**, 257–263.

82 S. Laurent, D. Forge, M. Port, A. Roch, C. Robic, L. Vander Elst and R. N. Muller, *Chem. Rev.*, 2008, **108**, 2064.

83 H. Amiri, R. Bustamante, A. Millan, N. J. O. Silva, R. Pinol, L. Gabilondo, F. Palacio, P. Arosio, M. Corti and A. Lascialfari, *Magn. Reson. Med.*, 2011, **66**, 1715–1721.

84 L. Lartigue, C. Innocenti, T. Kalaivani, A. Awwad, M. M. Sanchez Duque, Y. Guari, J. Larionova, C. Guérin, J. L. G. Montero and V. Barragan-Montero, *J. Am. Chem. Soc.*, 2011, **133**, 10459–10472.

85 T. L. Doane, C. H. Chuang, R. J. Hill and C. Burda, *Acc. Chem. Res.*, 2011, **45**, 317–326.

86 P. Riello, P. Canton and G. Fagherazzi, *J. Appl. Crystallogr.*, 1998, **31**, 78–82.

87 E. D. Palik, *Handbook of Optical Constants of Solids*, Academic Press, 1985.